

# NUMERICAL EXPERIMENTS WITH A TWO-DIMENSIONAL HORIZONTAL VARIABLE GRID

RICHARD A. ANTHERS

National Hurricane Research Laboratory, ESSA, Miami, Fla.

## ABSTRACT

A two-dimensional horizontal variable grid is derived that has maximum resolution at the center and minimum resolution near the boundaries of the grid. By using the analytic transformation that defines the variable grid, the equations of motion for a free-surface model are transformed in terms of new independent space variables in a computational domain with constant resolution. Numerical experiments utilize the variable grid to (1) increase the domain size with a fixed resolution at the center and (2) increase the resolution at the center with a fixed domain size.

Several finite-difference analogs and three time-integration schemes are tested. For a given domain size and number of grid points, several variable grid experiments show superior results in the mass and momentum fields compared to constant grid results. Most variable grid experiments, however, show a small (less than 1 percent) increase in total energy after 2000 time steps due apparently to the presence of additional nonlinear terms in the forecast equations.

The results show that, although care must be taken with the nonlinear terms, the variable grid may be effectively used in certain physical problems to economically gain resolution at the center of the domain.

## 1. INTRODUCTION

In numerical modeling of atmospheric phenomena that have nonuniform variation in space such as cumulus clouds, hurricanes, or fronts, it is tempting to economize on the computer time and storage required for the calculations by utilizing a variable grid. For example, Estoque (1962), Kuo (1965), Yamasaki (1968*a*, 1968*b*), and Anthes (1970) have used variable radial grids in axisymmetric hurricane models.

Variable grids yield economic dividends in two-dimensional models; they become a necessity when the physical phenomena cited above are considered in three dimensions. For example, if a 10-km horizontal mesh is necessary to adequately resolve the inner region of a hurricane, arrays of  $161 \times 161$  for each variable are required to cover a domain of radius 800 km from the storm center with a constant grid. Even with the simplest three-level model and a most economic integration scheme, this number of grid points is economically prohibitive. For the hurricane problem, a 10-km resolution is not required over the whole domain; in fact, 50 km or more may be sufficient to describe the hurricane structure beyond a radius of a few hundred kilometers.

In the circularly symmetric hurricane models, the introduction of a variable horizontal grid presents relatively few problems. By gradually increasing the separation of grid points in the radial direction, the orthogonality of the horizontal coordinates is preserved. With two horizontal dimensions, however, it is difficult to produce a simple orthogonal grid with a gradual increase in mesh length away from the center. This paper presents experiments with a free-surface model using a nonorthogonal variable horizontal grid designed primarily for the hurricane modeling problem. This grid possesses the following

properties:

1. The mesh size, in both north-south,  $y$ , and east-west,  $x$ , directions varies smoothly from a minimum value at the center of the domain to a maximum value along the boundary.

2. The variable grid is derived from an analytical transformation so that the "degree of variability" may be easily changed.

3. In the limiting case, the variable grid collapses to the familiar two-dimensional rectangular grid.

4. The distortion associated with the nonorthogonality of the variable grid is minimum at the center and maximum along the boundaries.

5. The programming of the model is straightforward.

It should be noted that the use of a variable grid is an attempt to resolve the dilemma between the physical requirement of high resolution in one portion of the domain and the economic impossibility of covering the entire domain with a constant grid of this high resolution. Of course, a constant grid with fine resolution would be superior to a variable grid with fine resolution over only a portion of the domain and coarser resolution elsewhere.

The following sections describe the variable grid, the physical model used to test the grid, and a number of numerical experiments.

## 2. THE VARIABLE GRID

The variable grid is derived from a continuous transformation mapping a horizontal domain,  $D'$  with coordinates  $x'$  and  $y'$ , into the horizontal domain  $D$  with coordinates  $x$  and  $y$ . Domain  $D$  corresponds to the normal physical space. The equations defining the transformation are

$$x = [C_1 + C_2(x'^2 + y'^2)^{1/2}]x' \quad (1)$$

and

$$y = [C_1 + C_2(x'^2 + y'^2)^{1/2}]y' \quad (2)$$

where  $C_1$  and  $C_2$  are arbitrary constants that determine the degree of variability of the grid. Note for  $C_1=1$  and  $C_2=0$  the variable grid collapses to the normal Cartesian grid. The Cartesian grid mesh points,  $x_{ij}$  and  $y_{ij}$ , are defined for an  $N \times M$  mesh by

$$x_{ij} = [C_1 + C_2(x_j'^2 + y_i'^2)^{1/2}]x_j', \quad (3)$$

$$y_{ij} = [C_1 + C_2(x_j'^2 + y_i'^2)^{1/2}]y_i', \quad (4)$$

$$x_j' = \left(j - \frac{N-1}{2}\right)\Delta x' \quad j=1, \dots, N, \quad (5)$$

and

$$y_i' = \left(\frac{M-1}{2} - i\right)\Delta y' \quad i=1, \dots, M \quad (6)$$

where  $\Delta x'$  and  $\Delta y'$  are the constant grid increments in the  $D'$  domain. In all experiments,  $N=M$  and  $\Delta x'=\Delta y'$ , so that the variable grid is symmetric in  $x'$  and  $y'$ . The increment  $\Delta x'$  corresponds to the minimum  $\Delta x$  in the  $D$  domain. In determining the properties of the variable grid, it is convenient to define the size of the domain by a single variable,  $R_{max}$ , that is the radius of the largest circle that can be inscribed in the domain covered by the variable grid. This parameter and the minimum grid increment,  $\Delta x'$ , determine the constants  $C_1$  and  $C_2$  (for the  $N \times N$  grid):

$$C_2 = \left(\frac{R_{max}}{\frac{1}{2}(N-1)\Delta x'} - 1\right) / \left[\frac{1}{2}(N-3)\Delta x'\right] \quad (7)$$

and

$$C_1 = 1 - C_2\Delta x'. \quad (8)$$

A typical example of the variable grid is shown in figure 1 for  $N=41$ ,  $\Delta x'=20$  km, and  $R_{max}=800$  km. The resolution varies from 20 km at the center to about 60 km at the corner of the domain.

At least two approaches to the computational problem with the variable grid are possible. The "box method" of Kurihara and Holloway (1967) offers one possibility. An alternative approach, and the one treated here, is to transform the model equations into their corresponding forms with  $x'$  and  $y'$  as independent variables. These new equations then apply to an orthogonal mesh in  $x'$ ,  $y'$  space with constant grid increments  $\Delta x'$  and  $\Delta y'$ , and the finite-differencing problem may be attacked along familiar lines.

### 3. THE FREE-SURFACE MODEL

The physical model used to test the variable grid is a free-surface model of an inviscid, incompressible fluid vortex that is confined in a more or less rectangular domain. The forecast equations consist of equations of motion for the horizontal velocity components and the continuity equation. The equations, written in a form

used by Smagorinsky et al. (1965), are

$$\frac{\partial hu}{\partial t} = -\frac{\partial hu u}{\partial x} - \frac{\partial hu v}{\partial y} + fhw - hg \frac{\partial h}{\partial x}, \quad (9)$$

$$\frac{\partial hv}{\partial t} = -\frac{\partial hu v}{\partial x} - \frac{\partial hu v}{\partial y} - fhu - hg \frac{\partial h}{\partial y}, \quad (10)$$

and

$$\frac{\partial h}{\partial t} = -\frac{\partial hu}{\partial x} - \frac{\partial hu}{\partial y} \quad (11)$$

where the velocities  $u$  and  $v$  are in the  $x$  and  $y$  directions on an  $f$  plane, respectively,  $h$  is the height of the fluid,  $g$  is the acceleration of gravity ( $9.81 \text{ m sec}^{-2}$ ), and  $f$  is the Coriolis parameter ( $5 \times 10^{-5} \text{ sec}^{-1}$ ).

The transformed equations corresponding to (9) through (11) in the  $x'$ ,  $y'$  coordinate system are obtained from the following expressions

$$\frac{\partial F}{\partial x} = \frac{\partial F}{\partial x'} \frac{\partial x'}{\partial x} + \frac{\partial F}{\partial y'} \frac{\partial y'}{\partial x} \quad (12)$$

and

$$\frac{\partial F}{\partial y} = \frac{\partial F}{\partial x'} \frac{\partial x'}{\partial y} + \frac{\partial F}{\partial y'} \frac{\partial y'}{\partial y} \quad (13)$$

where  $F$  is any quantity. It is convenient to treat the Jacobian terms, which are functions only of space, as map scale factors. These terms, computed from equations (1) and (2), are

$$M11 = \frac{\partial x'}{\partial x} = C/(AC - B^2),$$

$$M12 = \frac{\partial y'}{\partial x} = -B/(AC - B^2),$$

$$M21 = \frac{\partial x'}{\partial y} = -B/(AC - B^2),$$

and

$$M22 = \frac{\partial y'}{\partial y} = A/(AC - B^2) \quad (14)$$

where

$$A = C_2(x'^2 + y'^2)^{1/2} + C_2x'^2(x'^2 + y'^2)^{-1/2} + C_1,$$

$$B = C_2x'y'(x'^2 + y'^2)^{-1/2},$$

and

$$C = C_2(x'^2 + y'^2)^{1/2} + C_2y'^2(x'^2 + y'^2)^{-1/2} + C_1. \quad (15)$$

From the symmetry of the grid, the following relationships hold between the map scale factors:

$$M12_{ij} = M21_{ij}$$

and

$$M11_{ij} = M22_{ji}. \quad (16)$$

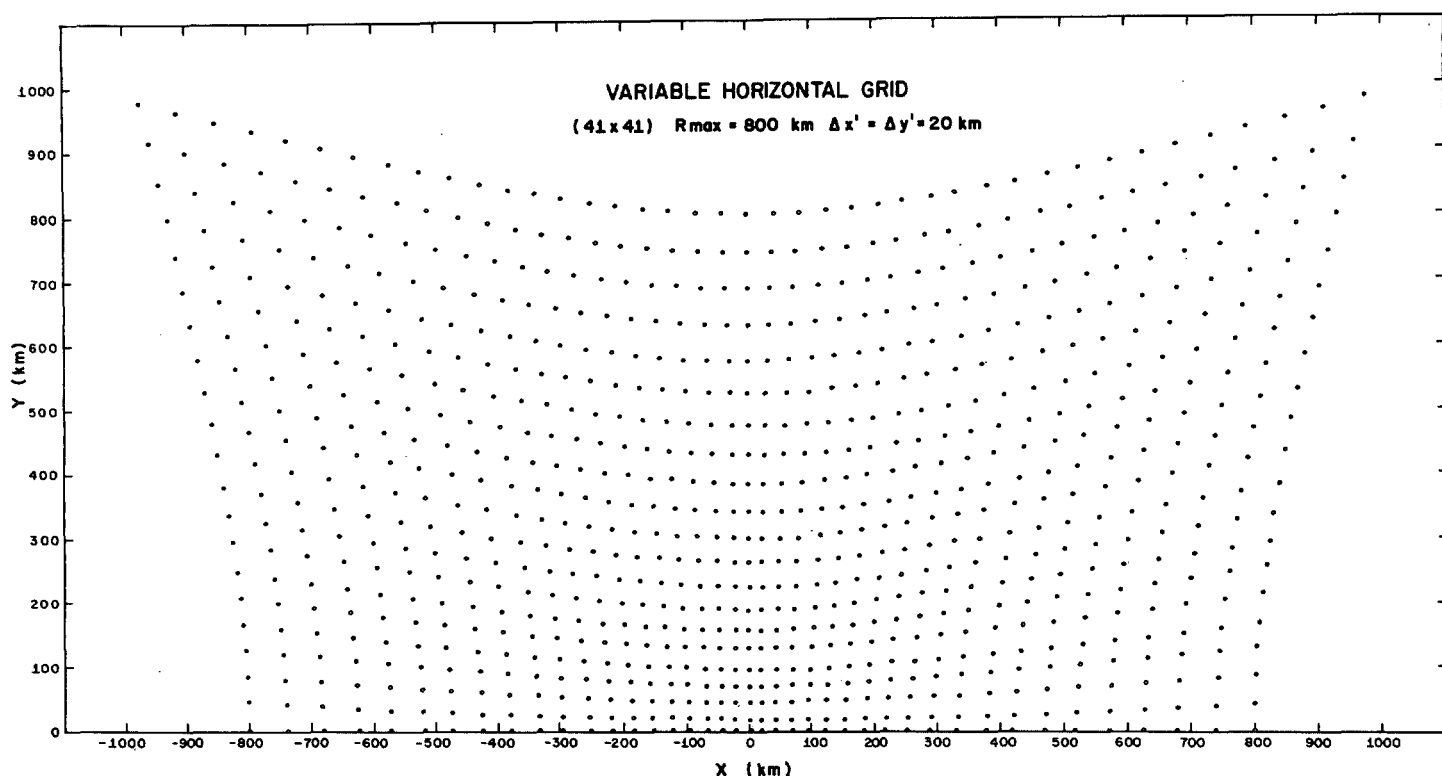


FIGURE 1.—Northern half of the variable grid defined by  $R_{max}=800$  km,  $\Delta x'=\Delta y'=20$  km.

The transformed model equations, using (12) through (14), are

$$\begin{aligned} \frac{\partial hu}{\partial t} = & - \left( M_{11} \frac{\partial hu^2}{\partial x'} + M_{12} \frac{\partial hu^2}{\partial y'} \right) \\ & - \left( M_{21} \frac{\partial huv}{\partial x'} + M_{22} \frac{\partial huv}{\partial y'} \right) + fhv \\ & - hg \left( M_{11} \frac{\partial h}{\partial x'} + M_{12} \frac{\partial h}{\partial y'} \right), \end{aligned} \quad (9')$$

$$\begin{aligned} \frac{\partial hv}{\partial t} = & - \left( M_{11} \frac{\partial huv}{\partial x'} + M_{12} \frac{\partial huv}{\partial y'} \right) \\ & - \left( M_{21} \frac{\partial hv^2}{\partial x'} + M_{22} \frac{\partial hv^2}{\partial y'} \right) - fhu \\ & - hg \left( M_{21} \frac{\partial h}{\partial x'} + M_{22} \frac{\partial h}{\partial y'} \right), \end{aligned} \quad (10')$$

and

$$\frac{\partial h}{\partial t} = - \left( M_{11} \frac{\partial hu}{\partial x'} + M_{22} \frac{\partial hu}{\partial y'} \right) - \left( M_{21} \frac{\partial hv}{\partial x'} + M_{12} \frac{\partial hv}{\partial y'} \right). \quad (11')$$

Equations (9') through (11') are now in terms of the constant, square grid  $D'$  but contain additional nonlinear terms that result from the nonorthogonality of the grid points in real space.

For a closed domain, the model equations conserve total energy  $E$  that consists of the sum of kinetic energy ( $K$ ) and potential energy ( $P$ ). These quantities are

$$E = K + P, \quad (17)$$

$$K = \frac{1}{2} \int_{\sigma} (u^2 + v^2) h d\sigma, \quad (18)$$

and

$$P = \frac{1}{2} g \int_{\sigma} h^2 d\sigma \quad (19)$$

where  $\sigma$  denotes area.

The available potential energy,  $A$ , is defined by

$$A = P - \frac{\sigma g \bar{h}^2}{2} = \frac{1}{2} g \int_{\sigma} \frac{h'^2}{2} d\sigma \quad (20)$$

where the overbar operator is

$$(\bar{\phantom{x}}) \equiv \frac{1}{\sigma} \int_{\sigma} (\phantom{x}) d\sigma \quad (21)$$

and the prime symbol denotes departures from this area mean.

The relationship between integrals over the  $D$  and  $D'$  domains is

$$\iint_D F(x, y) dx dy = \iint_{D'} F(x', y') |J(x', y')| dx' dy' \quad (22)$$

where the Jacobian of transformation is

$$J(x', y') = \det \begin{bmatrix} \frac{\partial x}{\partial x'} & \frac{\partial y}{\partial x'} \\ \frac{\partial x}{\partial y'} & \frac{\partial y}{\partial y'} \end{bmatrix} \quad (23)$$

$$= AC - B^2 = (M_{11} M_{22} - M_{12}^2)^{-1}. \quad (24)$$

The finite-difference form of equation (22) used to evaluate (18) and (20) is

$$\iint_{D'} F(x', y') |J(x', y')| dx' dy' \approx \Delta x' \Delta y' \sum_{i=2}^{N-1} \sum_{j=2}^{N-1} \frac{F_{ij}}{M11_{ij} M11_{ji} - M12_{ij}^2} \quad (25)$$

### ERROR ANALYSIS FOR VARIABLE GRID

To compare the relative truncation errors from the constant and variable grids, consider the term  $\partial F / \partial x$  and its transformation in one dimension,  $M11(\partial F / \partial x')$ . For a constant grid, it is well known that centered differencing has second order accuracy, that is,

$$\frac{\partial F}{\partial x} = \frac{F_{j+1} - F_{j-1}}{2\Delta x} - \frac{\Delta x^2}{6} \frac{\partial^3 F}{\partial x^3}(\xi) \quad (26)$$

where  $\xi$  is some point between  $x_{j-1}$  and  $x_{j+1}$ . If the corresponding term is evaluated in the  $x'$  coordinate system, where again the spacing is uniform,

$$M11 \frac{\partial F}{\partial x'} = M11 \left( \frac{F_{j+1} - F_{j-1}}{2\Delta x'} \right) - \frac{\Delta x'^2}{6} \frac{\partial^3 F}{\partial x'^3}(\xi') \quad (27)$$

where  $\xi'$  is between  $x'_{j-1}$  and  $x'_{j+1}$ . For the transformation defined by equation (1), the relationship between  $\partial^3 F / \partial x^3$  and  $\partial^3 F / \partial x'^3$  is

$$M11 \frac{\partial^3 F}{\partial x'^3} = (2C_2 x' + C_1)^2 \frac{\partial^3 F}{\partial x^3} + 6C_2 \frac{\partial^2 F}{\partial x^2} \quad (28)$$

Thus the error in the constant grid,  $E_c$ , is bounded by

$$|E_c| \leq \frac{\Delta x^2}{6} \left| \frac{\partial^3 f}{\partial x^3}(\xi_{max}) \right| \quad (29)$$

and the error in the variable grid,  $E_v$ , is bounded by

$$|E_v| \leq \frac{\Delta x'^2}{6} \left| [(2C_2 x' + C_1)^2 \frac{\partial^3 F}{\partial x^3}(\xi'_{max}) + 6C_2 \frac{\partial^2 F}{\partial x^2}(\xi'_{2max})] \right| \quad (30)$$

where  $\xi_{max}$ , and  $\xi'_{1max}$ , and  $\xi'_{2max}$  are values in the appropriate intervals that maximize the second and third derivative terms. As expected, the accuracy of the centered differencing in the variable grid is no longer second order, and any gain in accuracy must result from the fact that  $\Delta x'^2 < \Delta x^2$ .

### FINITE-DIFFERENCE EQUATIONS

The finite-difference equations corresponding to (9') through (11') for the main set of experiments comprise the "total energy conservative momentum" scheme used by Grimmer and Shaw (1967) and tested as "scheme B" in

Grammeltvedt's (1969) paper.<sup>1</sup> In the present paper, this scheme is designated as "method I." In Shuman's (1962) notation

$$\alpha_x = \frac{1}{\Delta x} \left[ \alpha \left( x_j + \frac{\Delta x}{2} \right) - \alpha \left( x_j - \frac{\Delta x}{2} \right) \right] \quad (31)$$

$$\bar{\alpha}^x = \frac{1}{2} \left[ \alpha \left( x_j + \frac{\Delta x}{2} \right) + \alpha \left( x_j - \frac{\Delta x}{2} \right) \right],$$

the finite-difference equations are

$$\begin{aligned} \frac{\partial(hu)_{ij}}{\partial t} \approx & -[M11_{ij} (\bar{h}u^x \bar{u}^x)_x + M12_{ij} (\bar{h}u^y \bar{u}^y)_y] \\ & -[M12_{ij} (\bar{h}v^x \bar{u}^x)_x + M11_{ji} (\bar{h}v^y \bar{u}^y)_y] \\ & + fhv_{ij} - gh_{ij} [M11_{ij} \bar{h}^x_x + M12_{ij} \bar{h}^y_y], \end{aligned} \quad (32)$$

$$\begin{aligned} \frac{\partial(hv)_{ij}}{\partial t} \approx & -[M11_{ij} (\bar{h}u^x \bar{v}^x)_x + M12_{ij} (\bar{h}u^y \bar{v}^y)_y] \\ & -[M12_{ij} (\bar{h}v^x \bar{v}^x)_x + M11_{ji} (\bar{h}v^y \bar{v}^y)_y] \\ & -fhu_{ij} - gh_{ij} [M12_{ij} \bar{h}^x_x + M11_{ji} \bar{h}^y_y], \end{aligned} \quad (33)$$

and

$$\begin{aligned} \frac{\partial h_{ij}}{\partial t} \approx & -[M11_{ij} \bar{h}u^x_x + M12_{ij} \bar{h}u^y_y] \\ & -[M12_{ij} \bar{h}v^x_x + M11_{ji} \bar{h}v^y_y]. \end{aligned} \quad (34)$$

In writing (32) through (34), we have used equation (16) and dropped the primes in the  $x'$  and  $y'$  notation for simplicity.

### INITIAL CONDITIONS

The initial conditions consist of a gradient vortex. The height field is computed from

$$H(r) = H_{rim} - \frac{100 \times 10^3}{r} \quad r \geq 20 \text{ km}$$

$$H(r) = 1000 \text{ m} \quad r \leq 20 \text{ km} \quad (35)$$

where  $H_{rim}$  is the height (1005 m in these experiments) of the "undisturbed" fluid at infinite distance from the center and  $r$  is the distance from the center. The  $u$  and  $v$  components are then computed from

$$u = -V_\lambda y/r \quad (36)$$

and

$$v = V_\lambda x/r$$

where  $V_\lambda$  is the tangential velocity computed from

$$V_\lambda = -\frac{fr}{2} + \frac{1}{2} \sqrt{f^2 r^2 + 4g \left( x \frac{\partial h}{\partial x} + y \frac{\partial h}{\partial y} \right)} \quad (37)$$

<sup>1</sup> Although the right-hand sides of equations (32) through (34) conserve total energy, truncation error in the time integration scheme may lead to changes in total energy, as pointed out by Grammeltvedt (1969).

with

$$\left(\frac{\partial h}{\partial x}\right)_{ij} \approx M11_{ij} \bar{h}'_x + M12_{ij} \bar{h}'_y, \quad (38)$$

and

$$\left(\frac{\partial h}{\partial y}\right)_{ij} \approx M12_{ij} \bar{h}'_x + M11_{ij} \bar{h}'_y.$$

Figure 2 shows the initial heights and the  $u$  components for the northern semicircle. This initialization scheme will generate rather large amplitude gravity waves initially, because the finite-difference equations do not satisfy the gradient wind equation. However, this feature is not particularly undesirable in these experiments because one of the objects is to test the behavior of high-frequency and small-scale disturbances on the variable grid.

#### 4. RESULTS

##### CONSTANT GRID EXPERIMENTS

The first series of experiments utilize a constant grid with 20-km resolution to study the effect of lateral boundary conditions, to compare the leapfrog time integration scheme with the Matsuno (1966) scheme, and to serve as a basis of comparison with the variable grid calculations. For a summary of all experiments, see table 1.

Experiments 1 and 2 compare results from two lateral boundary conditions. In experiment 1, the boundary conditions are chosen to yield zero mass change over the interior of the domain and so that the normal derivatives of the tangential component of the wind and the heights are zero along the boundary. The conditions are

$$\begin{aligned} V_{nB} &= -V_{nB+1}, \\ V_{tB} &= V_{tB+1}, \\ H_B &= H_{B+1} \end{aligned} \quad (39)$$

where the subscripts  $n$  and  $t$  represent normal and tangential components along the boundary, and  $B$  and  $B+1$  represent values on the boundary and at the adjacent interior grid points, respectively. In experiment 2, the values on the boundary are given for all time by the analytic steady-state solution of gradient balance. Both experiments utilize the leapfrog time integration scheme with a time smoothing operator (Smagorinsky et al. 1965) defined by

$$q^n = \frac{1}{4} (q^{n-1} + 2q^n + q^{n+1}) \quad (40)$$

where  $q$  is any forecast quantity and the superscripts refer to the time step. This smoothing is applied every 100 time steps to suppress the computational mode.

Figures 3 and 4 show the height fields after 1000 steps (25 hr) for experiments 1 and 2. Both distributions are irregular away from the center of the vortex. The heights associated with the analytic boundary conditions appear to be qualitatively closer to the initial (true) heights.

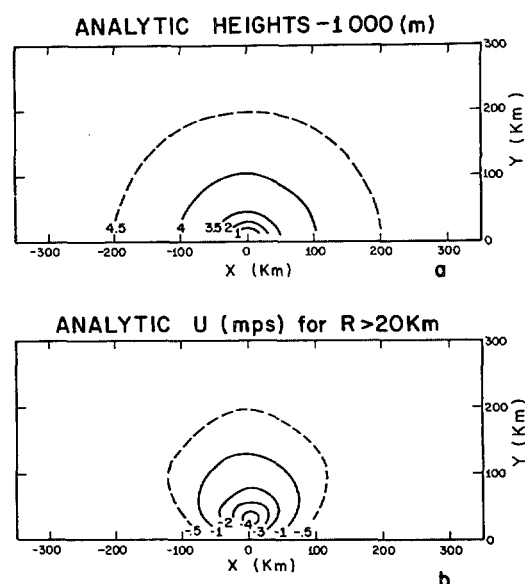


FIGURE 2.—Initial data for the northern half of the domain; (a) analytic heights minus 1000 m and (b) the east-west velocity component ( $u$ ) computed from the finite-difference analog to the gradient wind equation.

Compare figures 4 and 2a. The momentum structures in the two experiments are quite similar, as shown by the plot of the  $u$  component along the north-south axis in figure 5.

The time variation of the central height,  $h_0$ , and the energy budget for experiments 2 and 3 are shown in figure 6. Although the central height oscillations are greater in the case with analytic boundaries, the oscillations in the energy budget are greater in the case in which total mass is conserved exactly. The reasons for this paradox are obscure. Possibly the steady-state boundaries prevent large space oscillations from developing near the boundaries, resulting in smaller variations in the energy budget. The difference in the central height oscillations may be related to different reflective properties of the "walls."

Although experiment 2 with analytic boundaries does not conserve mass exactly,  $\bar{h}$  remains nearly constant with time, oscillating between 1004.5546 and 1004.5622, representing mass changes of less than 0.0005 percent. Because of the smoother height field in experiment 2, therefore, future experiments are computed with the analytic steady-state boundaries.

Both experiments 1 and 2, which utilize the leapfrog time integration scheme, show considerable small-scale irregularities in the height field after 1000 steps. The high-frequency oscillations in the central height (fig. 6a) suggest that these irregularities result from high-frequency gravity waves. The concentration of the energy in the short wavelengths is an undesirable result of nonlinear interactions in the equations.

The Matsuno (1966) integration scheme, although only of first-order accuracy, provides a selective time truncation, with high-frequency waves suffering the greatest damping. It has been used extensively by Leovy and

TABLE 1.—Summary of all experiments

Exp. no.	Min $\Delta x$ (km)	$R_{max}$ (km)	Grid type	$\Delta t$ (sec)	Boundary conditions	Time integration scheme	Space finite differences	Energy budget after 25 hr ( $10^{10} \text{ m}^2 \text{ sec}^{-2}$ )				
								$N$ steps	$\Delta K$	$\Delta A$	$\Delta(A+K)^\dagger$	Change (%)
1	20	400	C*	90	Mass-conservative	Leapfrog	Method I	1000	-3.0	-8.8	-11.8	-0.07
2	20	400	C	90	Analytic	"	"	1000	1.0	-8.3	-7.3	-.04
3	20	400	C	90	"	Matsuno	"	1000	-12.7	-5.1	-17.8	-.11
4	20	442	V	90	"	"	"	1000	-1.8	-5.1	-6.9	-.04
5	20	500	V	90	"	"	"	1000	14.2	-5.1	9.0	.05
6	20	600	V	90	"	"	"	1000	40.5	-5.0	35.6	.21
7	20	800	V	90	"	"	"	1000	72.2	-3.0	69.2	.40
8	20	1200	V	90	"	"	"	1000	34.1	4.4	38.5	.22
9	40	800	C	180	"	"	"	500	-18.4	-12.9	-31.3	-.21
10	10	800	V	45	"	"	"	2000	128.4	60.9	189.4	1.11
11	10	800	V	45	"	"	Box method continuity eq.	2000	66.3	.5	66.8	.39
12	10	800	V	45	"	"	Shuman avg.	2000	80.0	2.6	82.6	.48
13	10	800	V	45	"	Lax-Wendroff	Box method continuity eq.	2000	-5.4	-4.1	-9.6	-.06

\*C=constant and V=variable. †Because of roundoff, the sum of  $\Delta K$  and  $\Delta A$  may not exactly equal  $\Delta(A+K)$ .

MASS CONSERVATION  
N=1000  
T=25 HOURS  
H=1000 (m)

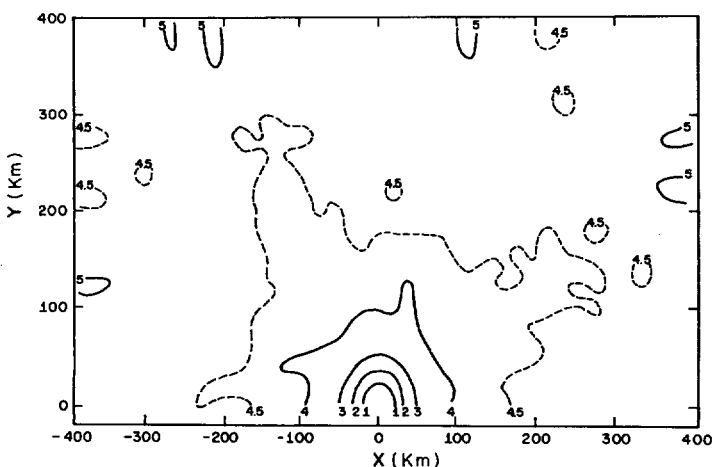


FIGURE 3.—Height field after 1000 steps (25 hr) for experiment 1 (constant grid, mass conservative boundaries).

Mintz (1969) in a general circulation model. If the irregularities in experiments 1 and 2 are due primarily to high-frequency waves, the Matsuno scheme should produce smoother fields. One step of the Matsuno scheme for one variable is summarized below for the equation  $\partial\alpha/\partial t = F(\alpha)$ :

1. Given  $\alpha^n$ ,
  2. Forecast first guess of  $\alpha^{n+1}$ , denoted by  $\alpha^*$ , from  $\alpha^* = \alpha^n + \Delta t F(\alpha^n)$ , and
  3. Forecast final estimate of  $\alpha^{n+1}$  by  $\alpha^{n+1} = \alpha^n + \Delta t F(\alpha^*)$ .
- Any improvement using the Matsuno scheme over the leapfrog scheme is at the expense of an increase by a factor of 2 in computational time.

Experiment 3 is identical to experiment 2, except that the Matsuno differencing scheme is utilized in experiment 3. Figure 7 shows the height field after 25 hr for experiment 3. Unlike the fields in experiments 1 and 2 (figs. 3 and 4), the height field in experiment 3 is very smooth and symmetric. The momentum fields (not shown) are also smoother.

ANALYTIC BOUNDARIES

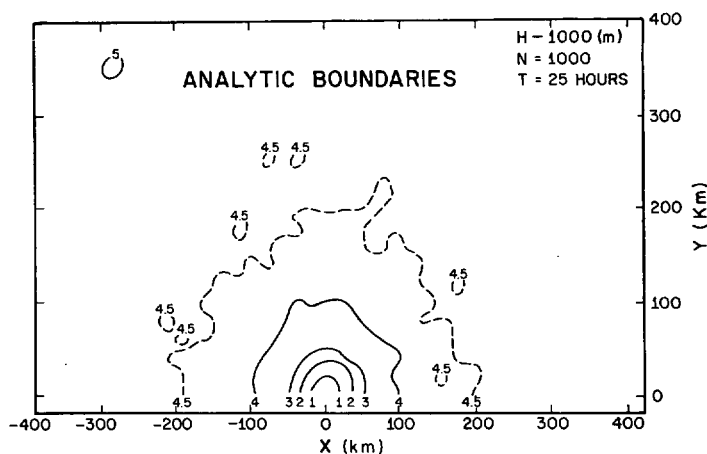


FIGURE 4.—Height field after 1000 steps (25 hr) for experiment 2 (constant grid, analytic, steady-state boundaries).

The high-frequency oscillations in central height and in the energy budget in experiment 2 are absent in experiment 3 (fig. 8). The damping of these high-frequency waves, while yielding smoother height fields, has little effect on the momentum profiles, as shown in figure 5. Thus, the Matsuno scheme is beneficial from a computational viewpoint without significantly altering the physically important solutions. Therefore, subsequent experiments utilize this time integration scheme.

#### VARIABLE GRID EXPERIMENTS

Two series of experiments are utilized to study the properties of the variable grid. The first approach studies the effects of changing domain size while holding the minimum space increment fixed at 20 km. The second approach studies the effect of changing the minimum resolution with a constant domain size of 800 km. In all cases, the number of grid points is the same ( $41 \times 41$ ).

#### VARIATION OF DOMAIN SIZE

In experiments 3 through 8 (table 1), the domain size defined by  $R_{max}$  is progressively increased from 400 km

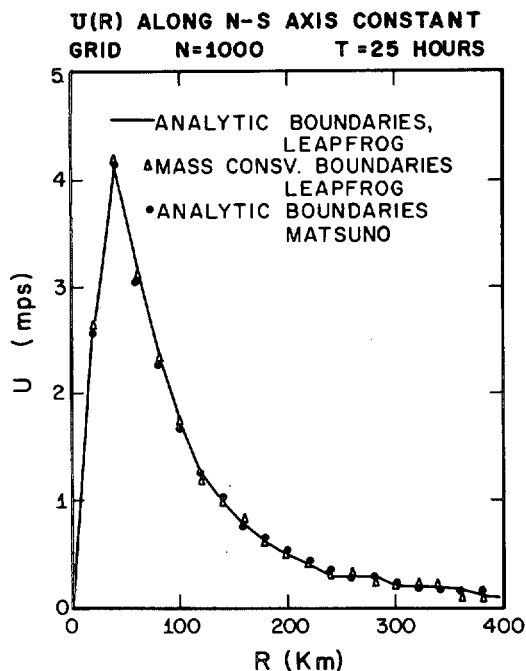


FIGURE 5.—Radial profile of the  $u$  component along the north-south axis for the constant grid after 1000 steps (25 hr) for experiments 1 (leapfrog, mass conservative boundaries), 2 (leapfrog, analytic boundaries), and 3 (Matsuno, analytic boundaries).

(constant grid) to 1200 km. The resolution at the center of the domain in these experiments is 20 km; thus the gain in domain size is accompanied by a loss in resolution away from the center. The profiles of the  $u$  component along the north-south axis after 25 hr (1000 steps) for experiments 3, 5, 7, and 8 are shown in figure 9. The variable grid calculations show good agreement with those for the constant grid.

Although the momentum profiles agree quite well, there are significant differences between the energy budgets associated with the constant and variable grids. Figure 10 shows the change from the initial values of the sum of available and kinetic energy for experiments 3 through 8. Whereas the change associated with the constant grid shows only slight oscillations, the changes associated with the variable grids show progressively increased amplitude as the distortion increases with increasing domain size. This increase in energy appears to be caused by the additional nonlinear terms that arise in the variable grid equations. *Note, however, that the maximum changes over 1000 steps are less than 1 percent of the original total, even for the 1200-km domain experiment.*

The results from experiments 3 through 8 suggest that the variable grid may be effectively used in certain cases to economically increase the size of the domain, at least for short integrations. The increase of energy in the shorter wavelengths associated with the additional nonlinear interactions in the variable grid cases, while undesirable, is fairly small, even though neither diffusion terms nor space smoothing has been used. It is probable that this difficulty would be less significant if a diffusive term were included in the equations or if a smoothing technique were used periodically to damp the short waves.

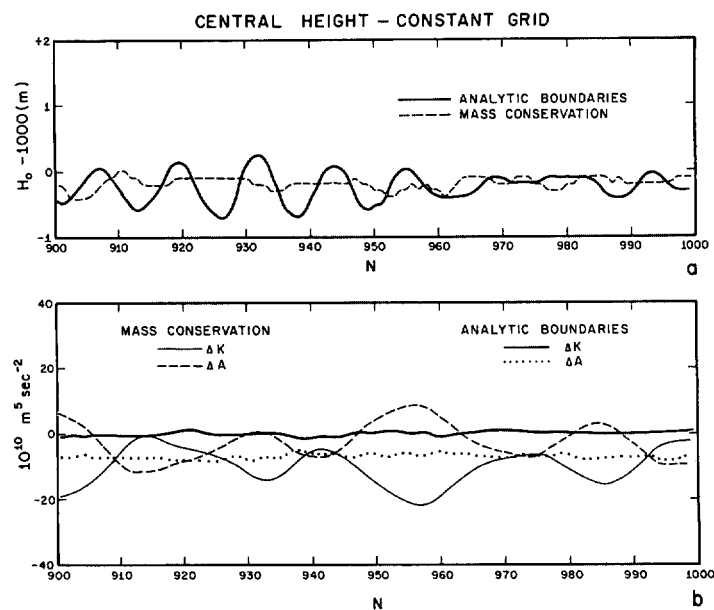


FIGURE 6.—(a) the central height for time steps 900–1000 for the constant grid experiments 1 (mass-conservative boundaries) and 2 (analytic boundaries); (b) the changes from initial values of kinetic and available potential energy for experiments 1 and 2.

#### VARIATION OF MAXIMUM RESOLUTION

In experiments 7, 9, and 10, the domain size remains constant at 800 km, and the maximum resolution at the center varies from 40 km (constant grid) to 10 km (table 1). The time step  $\Delta t$  varies according to

$$\frac{\Delta t}{\Delta x} = 4.5 \times 10^{-3} \text{ sec m}^{-1}.$$

Figure 11 shows the profiles of the  $u$  component along the north-south axis for the experiments with maximum resolution of 40, 20, and 10 km after 25 hr (500, 1000, and 2000 time steps, respectively). By comparison with the analytic profile beyond 20 km, the variable grid results are superior to the constant grid results in the inner 200-km region. Beyond 200 km, the profiles are nearly identical. Figure 12 shows the height fields for the 40- and 20-km maximum resolution cases. For the given domain size and number of grid points, the constant grid is unable to resolve the detail near the vortex center. The 4.5 contour is also more irregular in the constant grid case. Although the variable grid with resolution of 20 km shows substantial improvement in the height field, a further increase in maximum resolution to 10 km results in a deterioration in the height field (fig. 13) presumably due to an increase in distortion.

The  $u$  components (fig. 14) show further evidence of the superiority of the 20-km variable grid over the 40-km constant grid. Not only does the constant grid fail to resolve the easterly maximum near the center but also westerlies have appeared in several locations in the northern semicircle. In contrast, the variable grid shows easterlies throughout the northern semicircle and a maximum easterly velocity of over 3 m sec<sup>-1</sup>. The  $u$  components for the 10-km variable grid (not presented)

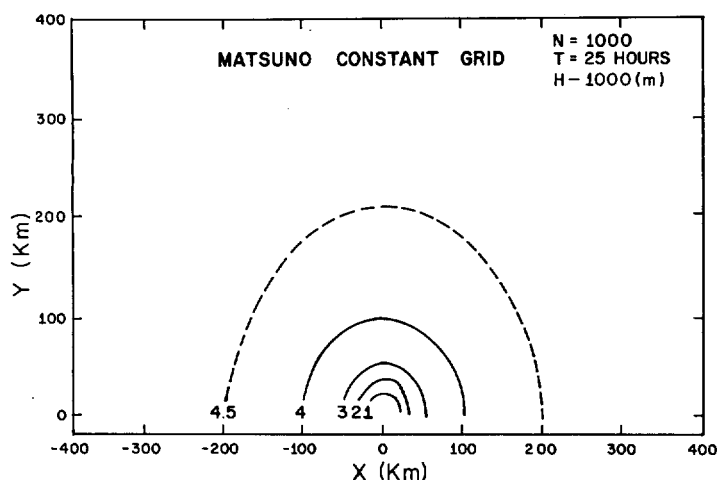


FIGURE 7.—Height field after 1000 steps (25 hr) for experiment 3 (constant grid, Matsuno integration scheme).

show additional improvement over the 20-km variable grid results by resolving a maximum of  $4.2 \text{ m sec}^{-1}$ .

The energy budget for experiments 7, 9, and 10 is summarized in figure 15. As in the experiments varying domain size, increased distortion of the variable grid produces a gradual increase in available potential and kinetic energy (see also table 1). The nearly monotonic increase in total energy associated with the 10-km maximum resolution experiment suggests that, without smoothing in space or diffusion terms, 2000 steps are about the limit of useful computations.

When summarizing the experiments with constant domain size, increasing the resolution near the center through the use of the variable grid from 40 to 20 and finally 10 km results in a substantial improvement in the velocity fields after 25 hr. The height distribution in the 20-km experiment is also qualitatively superior to the distribution in the 40-km experiment. In the 10-km experiment, however, increased nonlinear interactions produce a height distribution with space oscillations of wavelength  $2\Delta x$  and  $2\Delta y$  that lead to a large increase in the available potential energy.

The general success of the variable grid in accurately forecasting the mass and momentum for up to 2000 forecast steps warrants further effort to improve the behavior of the total energy budget, which shows a slow increase due to nonlinear effects. The next section examines additional differencing schemes and compares the results of each with those of experiment 10.

#### ADDITIONAL EXPERIMENTS WITH A TEN-KILOMETER VARIABLE GRID

In an effort to improve the behavior of the energy budget, experiment 10 is repeated with several different finite-differencing schemes and an additional time integration scheme. The selection of schemes is based on the results of the previous experiments and the experience of other investigators (for example, Shuman and Stackpole 1968 and Grammelvedt 1969). Experiment 10 is

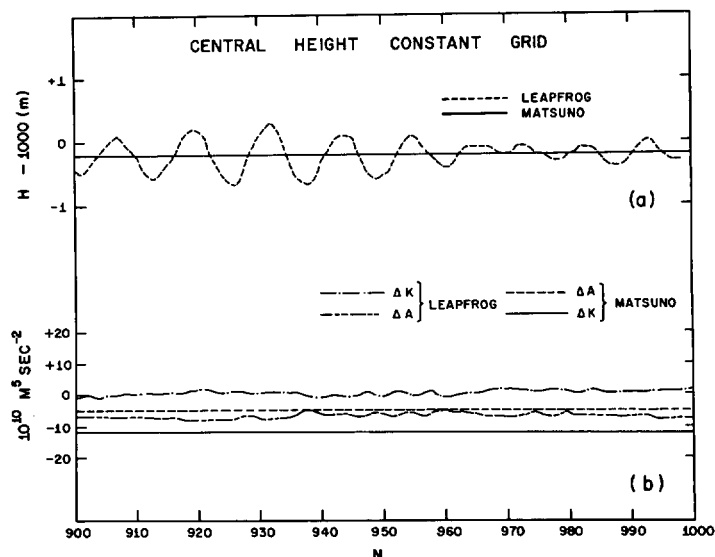


FIGURE 8.—(a) the central height for time steps 900–1000 for the constant grid experiments 2 (leapfrog) and 3 (Matsuno); (b) the changes from initial values of kinetic and available potential energy for experiments 2 and 3.

chosen as a standard for comparison because the behavior of the energy budget in this experiment was the worst of all the experiments.

The first alteration in the difference equations affects only the continuity equation and is suggested by noting that the primary contribution to the rapid increase in the total energy in experiment 10 beyond 1000 steps is the increase in available potential energy. We thus replace equation (34) with a finite-difference equation in flux form that conserves mass exactly and is analogous to Kurihara and Holloway's (1967) "box method." The complete set of equations is, therefore, no longer total energy conserving.

When considering the  $ij$ th grid point to be the center of a nonrectangular box, the continuity equation may be written as

$$\frac{\partial h}{\partial t} = \frac{hV_n s_1 + hV_n s_2 + hV_n s_3 + hV_n s_4}{\text{area of } ij\text{th box}} \quad (41)$$

where  $V_n$  is the component of the mean vector velocity that is normal to any particular side of length  $s_i$  of the box. The geometric relationships are

$$V_n = u_n + v_n, \quad (42)$$

$$u_n = B(A^2 + B^2)^{-1/2} u, \quad (43)$$

and

$$v_n = A(A^2 + B^2)^{-1/2} v$$

along the north-south sides of the box, and

$$u_n = C(C^2 + B^2)^{-1/2} u \quad (44)$$

and

$$v_n = B(C^2 + B^2)^{-1/2} v$$

along the east-west boundaries of the box.

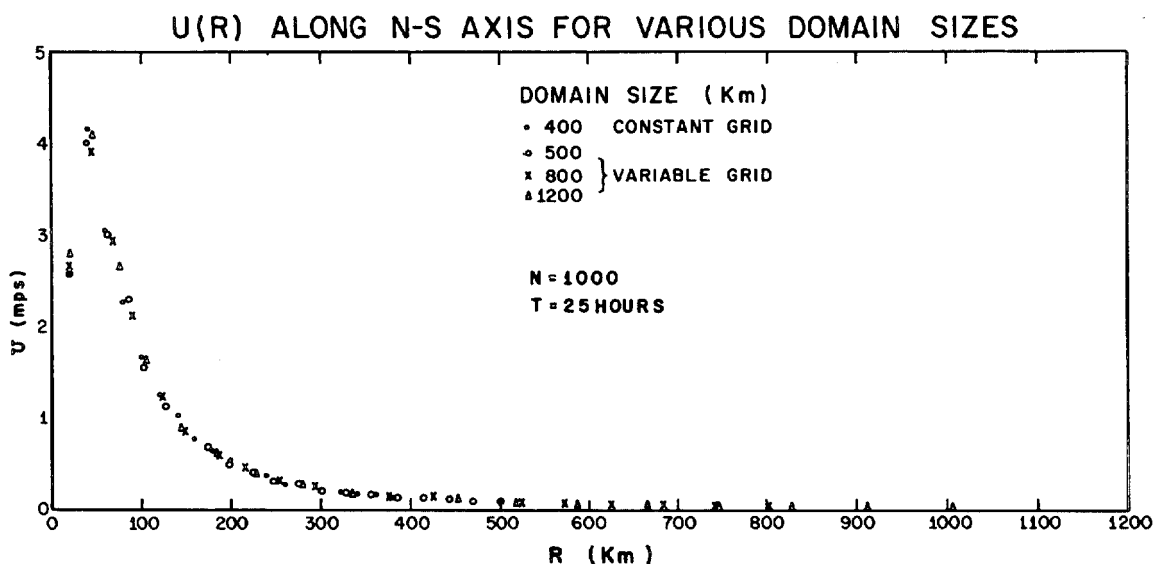


FIGURE 9.—Radial profiles of the  $u$  component along the north-south axis after 1000 steps (25 hr) for experiment 3 (constant grid,  $R_{max}=400$  km), experiment 5 (variable grid,  $R_{max}=500$  km), experiment 7 (variable grid,  $R_{max}=800$  km), and experiment 8 (variable grid,  $R_{max}=1200$  km).

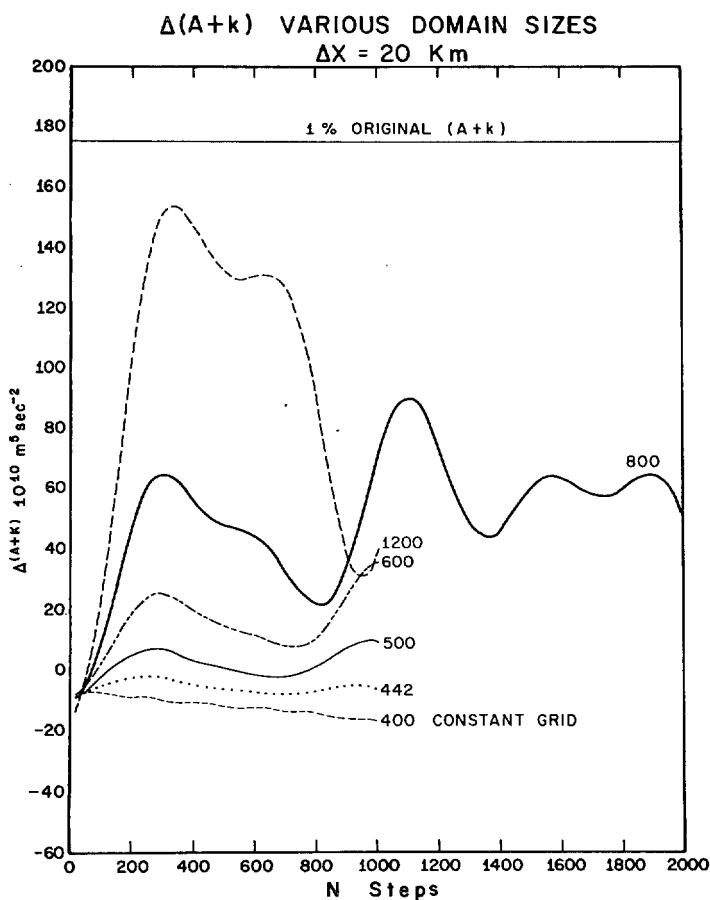


FIGURE 10.—Changes from initial value of the sum of kinetic and available potential energy for experiments investigating various domain sizes with a fixed central resolution of 20 km.

The length  $s_1$  is obtained from

$$s_1 = \int_{s_1} ds = \int_v \frac{ds}{dy'} dy' = \int_v (B^2 + C^2)^{1/2} dy', \quad (45)$$

$$s_1 \approx \overline{(B^2 + C^2)^{1/2}} \Delta y'.$$

Similarly,

$$s_2 \approx \overline{(A^2 + B^2)^{1/2}} \Delta x',$$

$$s_3 \approx \overline{(B^2 + C^2)^{1/2}} \Delta y', \quad (46)$$

$$s_4 \approx \overline{(A^2 + B^2)^{1/2}} \Delta x'.$$

and

The area of the  $ij$ th box is approximately

$$\text{area}_{ij} = (AC - B^2) \Delta x' \Delta y', \quad (47)$$

and the relationship of  $A$ ,  $B$ , and  $C$  to the map scale factors is

$$A = M22 / (M11 \ M22 - M12^2),$$

$$B = M12 / (M11 \ M22 - M12^2), \quad (48)$$

$$C = M11 / (M11 \ M22 - M12^2).$$

Substituting equations (42) through (46) into (41), the finite-difference form of the continuity equation becomes

$$\frac{\partial h}{\partial t_{ij}} \approx \left\{ \left[ -C_{i+j} \frac{u_{i+j+1} + u_{i+j}}{2} + B_{i+j} \frac{v_{i+j+1} + v_{i+j}}{2} \right] \Delta y' \right. \\ \left. + \left[ -A_{i-j} \frac{v_{i-j+1} + v_{i-j}}{2} + B_{i-j} \frac{u_{i-j+1} + u_{i-j}}{2} \right] \Delta x' \right. \\ \left. - \left[ -C_{i-j} \frac{u_{i-j} + u_{i-j-1}}{2} + B_{i-j} \frac{v_{i-j} + v_{i-j-1}}{2} \right] \Delta y' \right. \\ \left. - \left[ -A_{i+j} \frac{v_{i+j+1} + v_{i+j}}{2} \right. \right. \\ \left. \left. + B_{i+j} \frac{u_{i+j+1} + u_{i+j}}{2} \right] \Delta x' \right\} / (AC - B^2)_{ij} \Delta x' \Delta y'. \quad (49)$$

Experiment 11 is identical to experiment 10 except that equation (49) replaces (34) in computing the height tendencies. The energy budget of experiments 11 and 10 may be compared in figure 15. Although the total energy increases gradually in experiment 11, the rapid increase after 1000 steps found in experiment 10 (due primarily to the increase in available potential energy) is not pres-

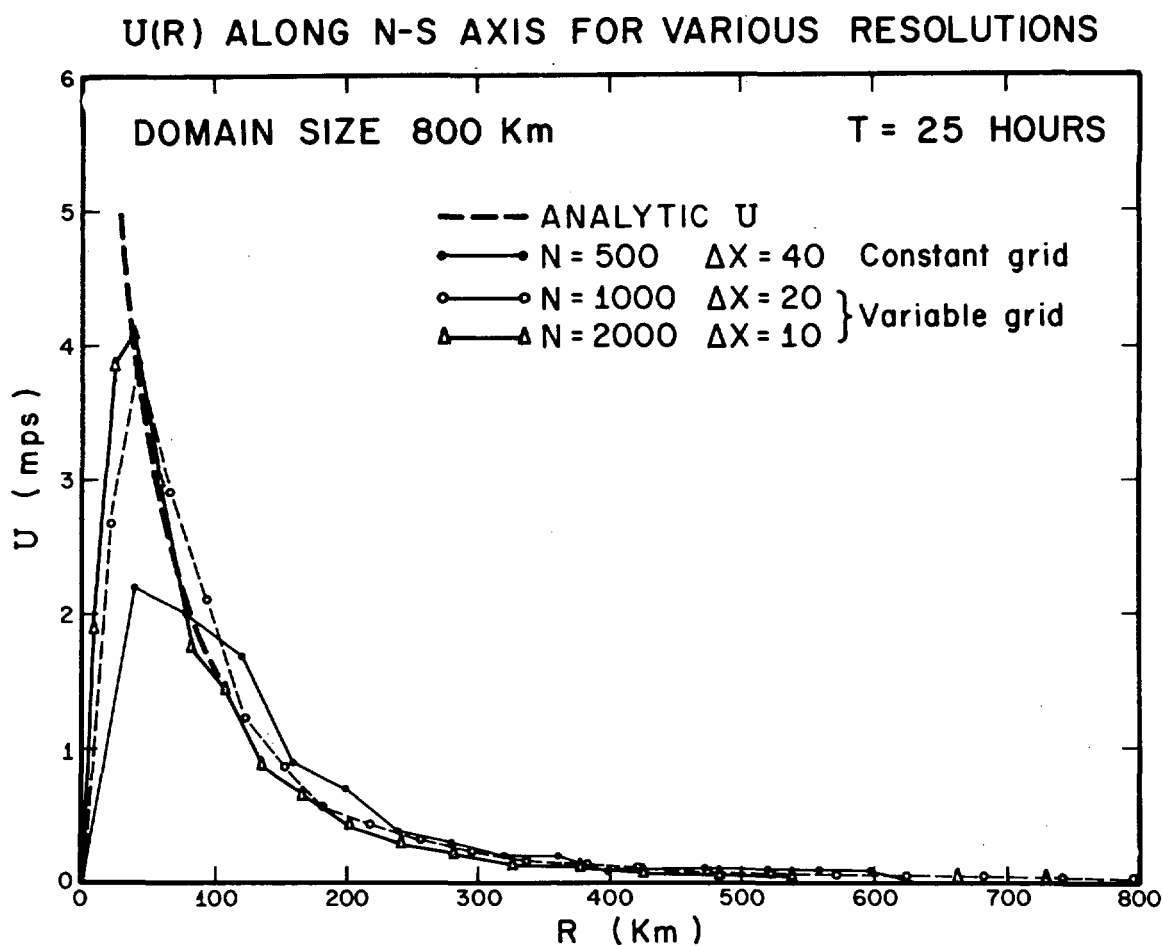


FIGURE 11.—Radial profile of the  $u$  component along the north-south axis after 25 hr for experiments 9 (constant grid, resolution=40 km) 7 (variable grid, maximum resolution=20 km), and 10 (variable grid, maximum resolution=10 km).

ent in experiment 11. Note that the change in available potential energy in experiment 11 is 0.5 unit compared to 60.9 units in experiment 10 (table 1). The amplitude of the  $2\Delta x$  and  $2\Delta y$  oscillations in the height field (not shown) are reduced from about 0.5 m in experiment 10 to less than 0.1 m in experiment 11. The use of the box method in representing the continuity equation, therefore, results in a substantial improvement in the forecasting of the height field, with no additional computation time.

The third set of finite-difference equations tested is an averaging scheme used by Shuman and Vanderman (1966) and found to give very good results as "scheme H" in Grammelvedt's (1969) series of experiments. This method essentially consists of averaging  $x$ -differentiated quantities over  $y$ ,  $y$ -differentiated quantities over  $x$ , and undifferentiated quantities over  $x$  and  $y$ . The finite-difference analog to equation (9') is

$$\begin{aligned} \frac{\partial hu}{\partial t} = & - \left[ \overline{M11}^{xy} \overline{(hu)u_x}^{xy} + \overline{M12}^{xy} \overline{(hu)u_y}^{xy} \right] \\ & - \left[ \overline{M21}^{xy} \overline{(hu)v_x}^{xy} + \overline{M22}^{xy} \overline{(hu)v_y}^{xy} \right] + \overline{fhu}^{xy} \\ & - \overline{gh}^{xy} \left( \overline{M11}^{xy} \overline{h_x}^{xy} + \overline{M12}^{xy} \overline{h_y}^{xy} \right); \end{aligned} \quad (50)$$

the forms corresponding to (10') and (11') are analogous and are not presented.

Experiment 12 is identical to experiment 10 except that the Shuman averaging scheme is used for all three forecast equations. The energy budget for experiment 12 is shown in figure 15 and summarized in table 1. An improvement over experiment 10 is again evident in both the kinetic and available potential energy budgets. However, the results are slightly inferior to experiment 11. The averaging scheme has the disadvantage of requiring about twice as much computing time as either of the previous differencing schemes. This twofold increase does not seem to be warranted from a comparison of experiments 10, 11, and 12.

In the final experiment, the two-step Lax-Wendroff time-integration scheme is used instead of the Matsuno scheme. This scheme has second-order accuracy, but contains some damping, especially for the short wavelengths (Richtmyer 1963). One cycle of this scheme, which is twice as fast as the Matsuno scheme, is summarized below for the equation  $\partial\alpha/\partial t = F(\alpha)$ :

1. Given  $\alpha^n$ .
2. Compute the first step according to  $\alpha^{n+1} = \overline{\alpha^n}^{xy} + \Delta t \times F(\alpha^n)$ .
3. Compute the second step according to  $\alpha^{n+2} = \alpha^n + 2\Delta t F(\alpha^{n+1})$ .

Experiment 13 is identical to experiment 11 (table 1) except that the two-step Lax-Wendroff scheme is used instead of the Matsuno scheme. The energy budget for

experiment 13 is shown in figure 15 and summarized in table 1. In contrast to previous variable grid experiments, the energy budget decreases monotonically through 1800 steps, with only a slight increase thereafter. After 2000

steps, the changes from the initial values of both the available potential and kinetic energy are negative and less than 0.1 percent of the initial values. The shortwave damping properties of the two-step Lax-Wendroff scheme appear, therefore, to improve the stability of the calculations by preventing the rapid accumulation of energy in the  $2\Delta x$  and  $2\Delta y$  wavelengths. At the same time, the large-scale height and velocity distributions (not shown) are in good qualitative agreement with the true steady-state solutions.

## 5. SUMMARY

A two-dimensional nonorthogonal variable grid is presented that has maximum resolution at the center and minimum resolution near the boundaries of the grid. The variable grid is derived from a continuous transformation that maps a rectangular computational domain,  $D'$ , into the physical  $x$ - $y$  domain,  $D$ , enabling the degree of variability to be easily changed in numerical experiments. By using this transformation, the equations of motion for a free-surface model are transformed in terms of the independent space variables in the computational domain  $D'$ . Numerical integrations with a fixed number of grid points utilize the variable grid to investigate (1) increasing the domain size with a fixed resolution at the center and (2) increasing the resolution at the center with a fixed domain size.

Three finite-difference analogs for the space derivatives and three time-integration schemes are tested for the variable grid. Preliminary results using the leapfrog time integration scheme yield inferior results because of the presence of high-frequency gravity waves. Most experiments were conducted using the Matsuno time integration

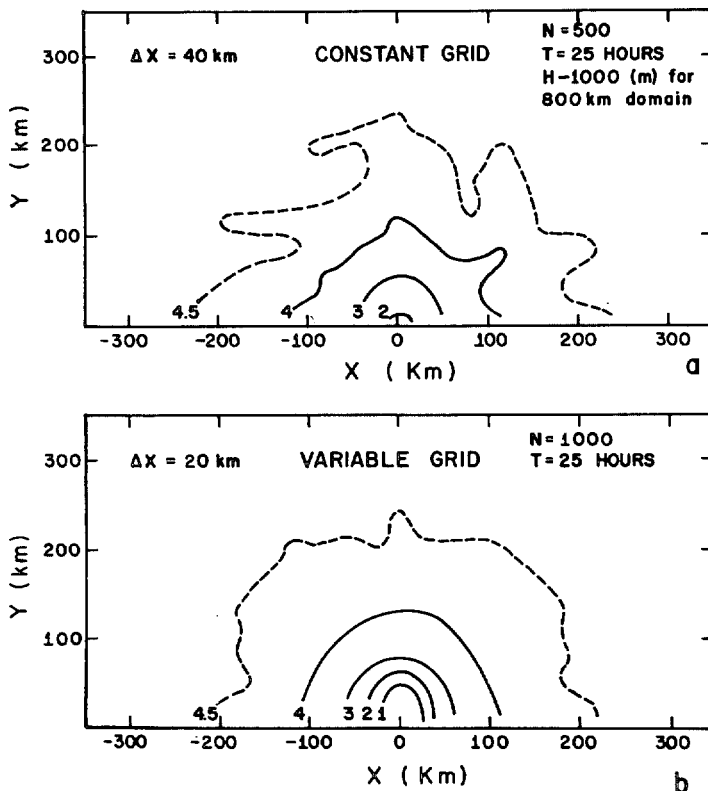


FIGURE 12.—(a) the height field after 25 hr (500 steps) for experiment 9 (constant resolution=40 km) and (b) the height field after 25 hr (1000 steps) for experiment 7 (variable grid, maximum resolution=20 km).

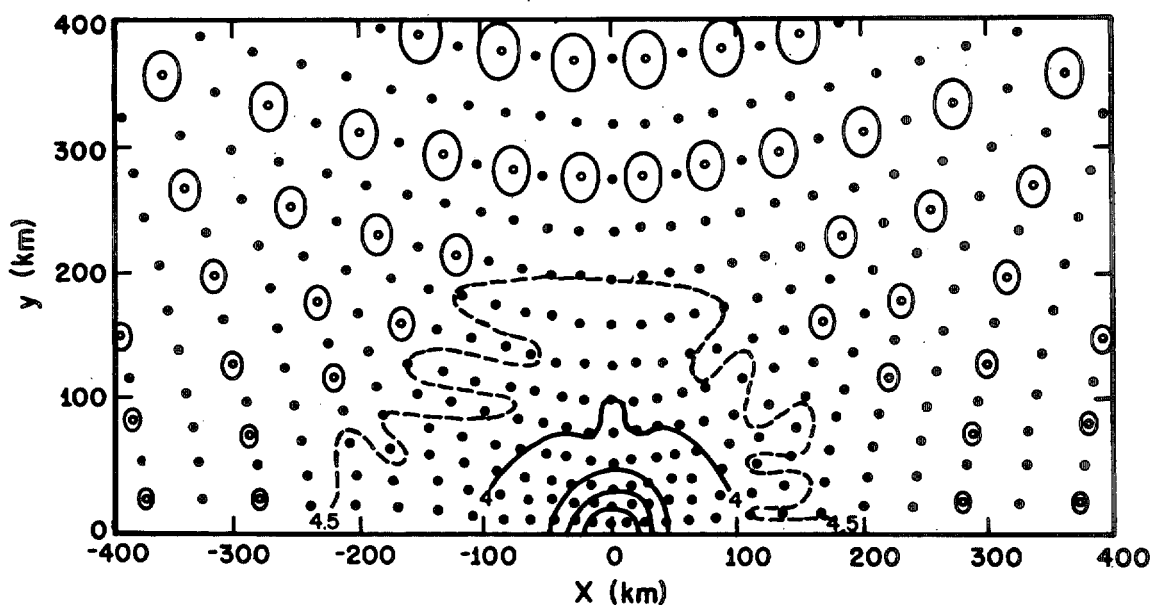


FIGURE 13.—Height field after 25 hr (2000 steps) for experiment 10 (variable grid, maximum resolution=10 km). All closed contours around a single grid point are in units of 5 m.

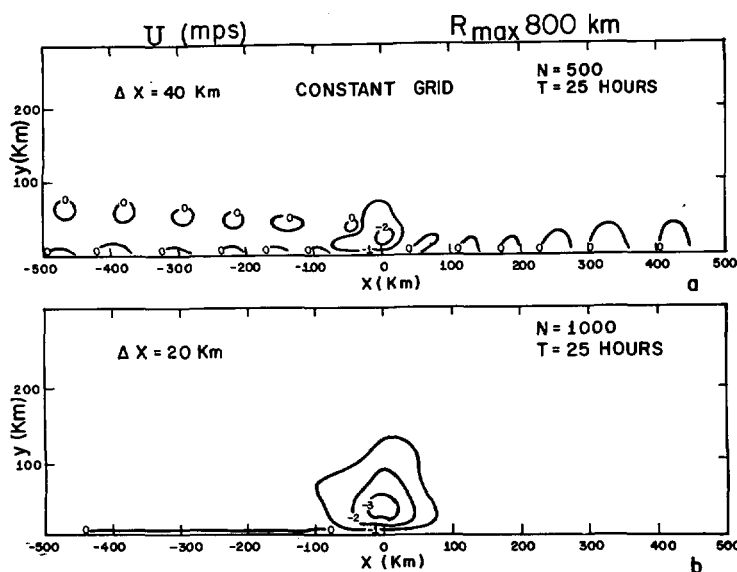


FIGURE 14.—(a) the  $u$  component field after 25 hr (500 steps) for experiment 9 (constant resolution=40 km) and (b) the  $u$  component field after 25 hr (1000 steps) for experiment 8 (variable grid, maximum resolution=20 km).

scheme which effectively filters the high-frequency waves. Most experiments utilize the total energy conservative momentum scheme (scheme B, Grammeltvedt 1969) for the finite-difference equations. All experiments are carried out to at least 1000 time steps.

For a fixed domain size and number of grid points, several variable grid experiments show qualitatively superior results in the mass and momentum fields compared to constant grid results. An undesirable feature of the variable grid experiments, however, is the gradual increase of total energy due to the accumulation of energy in the short wavelengths. This difficulty, which is caused by the additional nonlinear terms in the forecast equations, becomes more pronounced for the more distorted grids. However, in all but one experiment, the total energy change after 2000 time steps is less than 1 percent of the original energy.

Finally, the variable grid that has the maximum distortion is tested with two additional finite-difference schemes and one additional time integration scheme. Writing the continuity equation in a mass conservative form analogous to the box method yields a substantial improvement in the behavior of the available potential energy budget. Using an averaging scheme similar to Shuman and Vanderman's (1966) also yields an improvement, but at the expense of doubling the computational time. In the final experiment, the mass conservative form of the continuity equation and the two-step Lax-Wendroff time integration scheme yields very good results that show virtually no change in total energy over 2000 steps.

The experiments show, therefore, that although care must be taken with the nonlinear terms, the variable

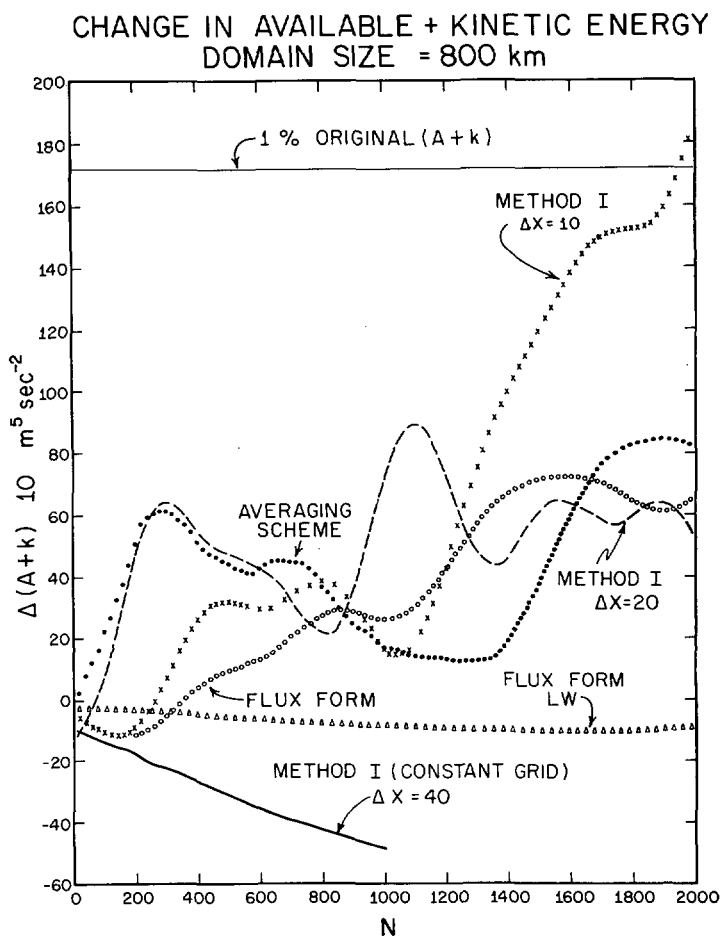


FIGURE 15.—Changes from initial value of the sum of kinetic and available potential energy for experiments 7 and 9 through 13. See table 1 for the summary of each experiment.

grid may be effectively used in certain physical problems to economically gain resolution at the center of the domain, at least for the time range considered here.

## REFERENCES

- Anthes, Richard A., "A Diagnostic Model of the Tropical Cyclone in Isentropic Coordinates," Ph. D. thesis, University of Wisconsin, Madison, 1970, 184 pp.
- Estoque, Mariano A., "Vertical and Radial Motions in a Tropical Cyclone," *Tellus*, Vol. 14, No. 4, Nov. 1962, pp. 394-402.
- Grammeltvedt, Arne, "A Survey of Finite-Difference Schemes for the Primitive Equations for a Barotropic Fluid," *Monthly Weather Review*, Vol. 97, No. 5, May 1969, pp. 384-404.
- Grimmer, M., and Shaw, D. B., "Energy-Preserving Integrations of the Primitive Equations on the Sphere," *Quarterly Journal of the Royal Meteorological Society*, Vol. 93, No. 397, July 1967, pp. 337-349.
- Kuo, H. L., "On the Formation and Intensification of Tropical Cyclones Through Latent Heat Release by Cumulus Convection," *Journal of the Atmospheric Sciences*, Vol. 22, No. 1, Jan. 1965, pp. 40-63.
- Kurihara, Yoshio and Holloway, J. Leith, Jr., "Numerical Integration of a Nine-Level Global Primitive Equations Model Formulated by the Box Method," *Monthly Weather Review*, Vol. 95, No. 8, Aug. 1967, pp. 509-530.

- Leovy, Conway, and Mintz, Yale, "Numerical Simulation of the Atmospheric Circulation and Climate of Mars," *Journal of the Atmospheric Sciences*, Vol. 26, No. 6, Nov. 1969, pp. 1167-1190.
- Matsuno, Taroh, "Numerical Integrations of the Primitive Equations by a Simulated Backward Difference Method," *Journal of the Meteorological Society of Japan*, Ser. 2, Vol. 44, No. 1, Feb. 1966, pp. 76-84.
- Richtmyer, Robert D., "A Survey of Difference Methods for Non-Steady Fluid Dynamics," *NCAR Technical Notes* 63-2, National Center for Atmospheric Research, Boulder, Colo., 1963, 25 pp.
- Shuman, Frederick G., "Numerical Experiments With the Primitive Equations," *Proceedings of the International Symposium on Numerical Weather Prediction, Tokyo, November 1960*, Meteorological Society of Japan, Tokyo, Mar. 1962, pp. 85-107.
- Shuman, Frederick G., and Stackpole, John D., "Note on the Formulation of Finite Difference Equations Incorporating a Map Scale Factor," *Monthly Weather Review*, Vol. 96, No. 3, Mar. 1968, pp. 157-161.
- Shuman, Frederick G., and Vanderman, Lloyd W., "Difference System and Boundary Conditions for the Primitive-Equation Barotropic Forecast," *Monthly Weather Review*, Vol. 94, No. 5, May 1966, pp. 329-335.
- Smagorinsky, Joseph, Manabe, Syukuro, and Holloway, J. Leith, Jr., "Numerical Results From a Nine-Level General Circulation Model of the Atmosphere," *Monthly Weather Review*, Vol. 93, No. 12, Dec. 1965, pp. 727-768.
- Yamasaki, Masanori, "Numerical Simulation of Tropical Cyclone Development With the Use of Primitive Equations," *Journal of the Meteorological Society of Japan*, Vol. 46, No. 3, June 1968a, pp. 178-201.
- Yamasaki, Masanori, "A Tropical Cyclone Model With Parameterized Vertical Partition of Released Latent Heat," *Journal of the Meteorological Society of Japan*, Vol. 46, No. 3, June 1968b, pp. 202-214.

[Received March 9, 1970; revised April 16, 1970]